

EXPERIMENTAL OBSERVATIONS OF CONCRETE BEHAVIOR UNDER UNIAXIAL COMPRESSION

Y-H. Lee, K. Willam, and H-D. Kang,
CEAE-Department, University of Colorado, Boulder, Colorado, USA

Abstract

This paper presents novel experimental observations of pre- and post-peak response phenomena when cylindrical concrete specimens are loaded under deformation control in uniaxial compression. Our focus are degradation measurements of stiffness and strength during unloading and reloading cycles considering the effects of boundary conditions on cylindrical specimens of different height. The existence of a unique focal point (pole) of stiffness degradation is explored for the description of elastic concrete degradation. The predominantly axial splitting failure is interpreted on the meso-level in order to overcome the shortcomings of macroscopic failure descriptions.

1 Introduction

Tensile fracture in cementitious materials such as mortar and con-

crete is normally studied in the form of mode I fracture experiments and in the form of direct and indirect tension tests. On the other hand well-posed mixed mode fracture studies are far scarcer, quite opposite to the standard compression test which is widely used for the characterization of mechanical concrete properties in spite of its index character. In fact, little effort has been expended to correlate the failure processes in tension and compression in order to extract more fundamental properties from post-peak measurements of stiffness and strength in uniaxial compression. The lack of quantitative experimental data has hampered the development of coupled elastic plastic damage formulations for concrete if one considers the date of the classic load-unload-reload compression tests by Sinha, Gerstle and Tulin (1964) at the University of Colorado, Boulder.

It is widely recognized (Van Mier 1984 and 1986, Vonk 1992, and Rokugo and Koyanagi 1992) that the degradation of strength and stiffness of concrete in uniaxial compression is accompanied by highly localized failure in the form of axial splitting. In contrast to the conical mode of shear failure, compressive splitting must resort to subtle explanations in terms of (a) fracture mechanics arguments considering initial microdefects (Nemat-Nasser and Hori, 1993), (b) mesomechanical arguments which account for the heterogeneity of concrete, and (c) boundary effects which induce tension along the line of the Brazilian test configuration. Slate and Hover (1984) showed pervasive internal crack growth up to peak by studying the interior of concrete specimens which were loaded up to a certain level and which were subsequently unloaded. From their experimental observations it is believed that energy dissipation in the pre-peak regime is a global continuum-dominated process which may be attributed to microcracking throughout the entire specimen. On the other hand, energy dissipation in the post-peak regime is a localized surface dominated fracture process after coalescence of macrocracks in the peak regime. In short, concrete failure in direct compression is a very complex process which entails tensile debonding due to mismatch in the aggregate-cement paste composite, as well as shear faulting in the form of crack bridging. Thereby the fundamental question is whether compressive failure is really another manifestation of tensile cracking, or an independent failure process of mixed

mode shear. The fracture argument is here addressed via the characteristic length argument which is observed from tests on specimens with different height.

Another issue in this paper is the identification of a unique focal point of stiffness degradation. This locus is determined using experimental observations between stiffness and strength, and between stiffness and permanent deformation. Through regression analysis of experimental data a secant relation is developed which paves the way to combine elastic degradation and plastic softening.

On a final note the axial splitting failure mode observed in the experiment is discussed in terms of the fracture mechanics of initial microdefects and microstructural argument which account for the heterogeneity of concrete. In this conjunction, shortcomings of macroscopic failure descriptions are contrasted with failure modes observed in experiments.

2 Experimental setup

2.1 Testing equipment

All experiments were carried out with a general purpose MTS compression and tension apparatus comprised of a standard 110 kips (489 kN) loading frame and function generator units. The averaged axial deformation measurements of two transducers which were attached between upper and lower loading platens were used as feedback signal for servo-control (Fig. 1(a)). The transducers were 200 hrdc LVDT with ± 0.2 inch nominal linear range and 15 V/inch sensitivity. Lateral deformations were measured by four transducers attached at midheight of the specimen at 90° intervals around the circumference (Fig. 1(b)). Four 100 hrdc LVDT with ± 0.1 inch nominal linear range and 54 V/inch sensitivity were used for this purpose. Data for all experiments were monitored and stored by a data acquisition system developed at the University of Colorado Structural Research Laboratory.

2.2 Test specimens

The tests were performed on cylindrical specimens of $d = 3.0$ in diameter and $h = 5.4, 3.6, 1.8$ in height. Normal strength and high strength concrete specimens were cast using two different mix

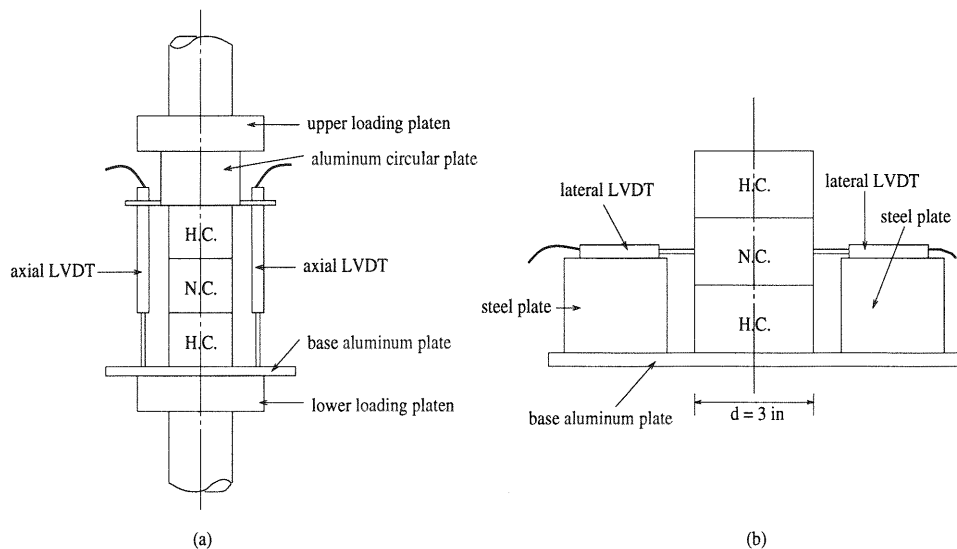


Figure 1: Test Set-up in Direct Compression Test (a): Axial transducers (b): Lateral transducers

proportions. The mix proportions resorted to a water-cement ratio of $W/C = 0.65$ and $W/C = 0.4$ for normal strength and high strength concrete, a mix of $C:S:G = 1:2.63:2.14$ and $1:1.28:1.31$ for normal and high strength concrete, and a maximum aggregate size of $d = 3/8$ in in both cases. ASTM C150 Type I Portland Cement was used. The cylinders were cast in steel molds and consolidated by hand tamping. The molds were removed approximately 24 hours after casting. The cylinders were then cured in a fog room until testing. The specimens, having an initial length of $H = 6$ in, were cut to their nominal lengths using a concrete saw. The ends of each specimen were milled with a diamond grinding wheel to the prescribed height with a tolerance of $\Delta H = \pm 0.02$ in.

2.3 Boundary conditions

The boundary condition in the uniaxial compression test depends primarily on the type of loading platen and the specific interface between specimen and loading platen. In the experiments fixed loading platens were used to stabilize the post-peak behavior. A very elaborate triaxial compression test set-up was developed by van Mier (1986) and by Vonk (1992) using steel brushes to minimize the interface friction. In the current compression test a special provision

was adopted to minimize the interface friction which was developed by Slowik et al. (1993) for direct tension tests. In their experiments the normal strength test cylinder was attached to two high strength concrete specimens of the same diameter. Since the elastic properties of the two concretes do not differ significantly, the lateral restraint at the end surfaces of the test specimen is minimized. Similarly to that tension set-up, the short test specimens ($h = 1.8$ in) were placed between two high strength concrete cylinders of 1.8 in height lubricating instead of gluing the platen interfaces (Fig. 1(a)). For the taller specimens ($h = 5.4$ and 3.6 in) the platen-specimen interfaces were prepared by lubrication with “grease”. The peak strengths of the three specimen geometries are summarized in Table 1 which indicates negligible difference of axial strength values. Without the special provision in Fig. 1, the $h = 1.8$ in specimen yielded $f'_c = 5.75$ ksi, which is 30% above the other values. In order to extract the deformation on the actual concrete specimen from the total deformation, a high strength specimen of 6.0 in height was tested up to 4.5 ksi under cyclic loading prior to the real test. The loading and unloading curves were approximated by 5th and 6th order polynomials through regression analysis. These calibrations were used to extract deformations of the normal strength specimen from axial LVDT readings depending on the loading condition.

Table 1: Peak strength and local fracture energies

Specimen height (inch)	Peak strength (ksi)	Stiffnesses (ksi) corresponding to stress levels at 4 ksi (pre-peak) and peak strength (ksi)				Local fracture energy ($kip \cdot in/in^2$)	
		4.0 (pre-peak)		peak strength		unloading	reloading
		unloading	reloading	unloading	reloading		
5.4	4.45	5200	3850	5200	2940	69.66	78.98
3.6	4.45	5130	3700	5130	2940	67.53	71.77
1.8	4.65	5080	3800	4900	2720	83.11	84.30

3 Experimental observations

3.1 Fracture energy effect

The post-peak behavior of concrete under uniaxial compression is a surface- dominated fracture process due to excessive lateral deformation which results in axial splitting. If the lateral restraint at the platen interface is minimized, this phenomenon is similar

to Mode I type tensile cracking in uniaxial tension except for the axial compression. In view of the constant fracture energy release rate argument in uniaxial tension, the question arises whether fracture energy is preserved in compression irrespective of specimen height. This question is studied with experiments on three specimen heights, $h = 5.4, 3.6,$ and 1.8 in ($1.8, 1.2,$ and 0.6 aspect ratio) with the same cross-section ($d=3$ in). During the test a constant deformation rate of 1.67×10^{-5} inch/sec was applied in all the tests irrespective of specimen height. Table 1 shows that the peak strength is independent of the specimen height due to the special provision in Fig. 1 for the $h = 1.8$ in specimen. Fig. 2 illustrates the nominal stress versus axial and lateral strain response of the three specimen heights. It indicates close agreement of stiffness up to

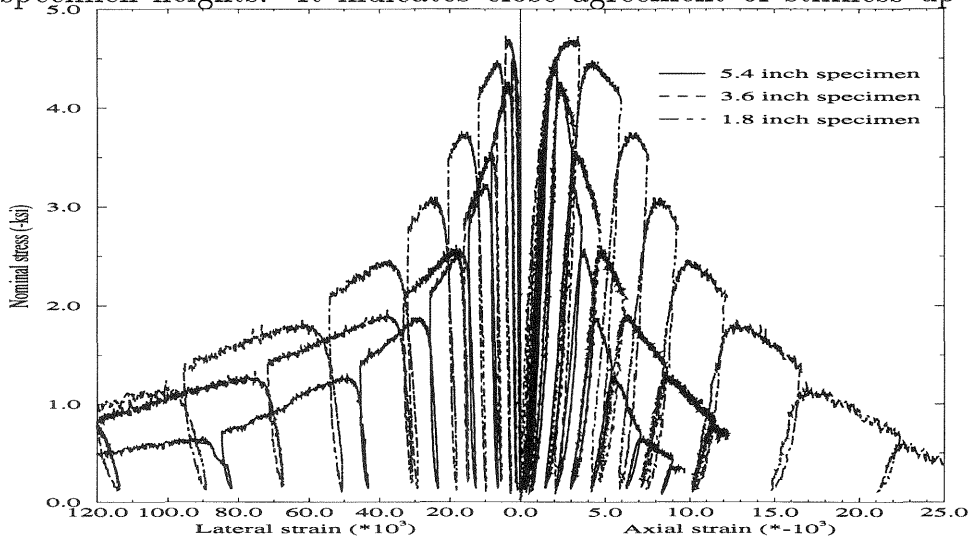


Figure 2: Nominal Stress vs. Axial and Lateral Strains

peak strength when interface friction is minimized, while the post-peak behavior diverges for the three specimen heights. The $h = 1.8$ in specimen failed by axial splitting within concentric rings of the cylindrical specimens intersected orthogonally by radial cracks. In addition, the axial splitting mode of the short test specimen penetrated the high strength concrete caps at both ends. Fig. 3 illustrates the nominal stress versus axial and lateral deformation response. In contrast to Fig. 2 the agreement of the post-peak behavior supports the argument of fracture energy irrespective of the specimen height. The local fracture energy values are listed in Table 1 which were extracted from the area in the post-peak regime

depending on the loading and unloading stiffnesses at peak strength (see Fig. 4).

The lateral deformations provide an another key to probe the constant fracture energy release rate in the post-peak regime as a function of specimen height. Fig. 5 illustrates lateral versus axial deformations and lateral versus axial strains, where the lateral strain values were obtained by dividing averaged values of two lat-

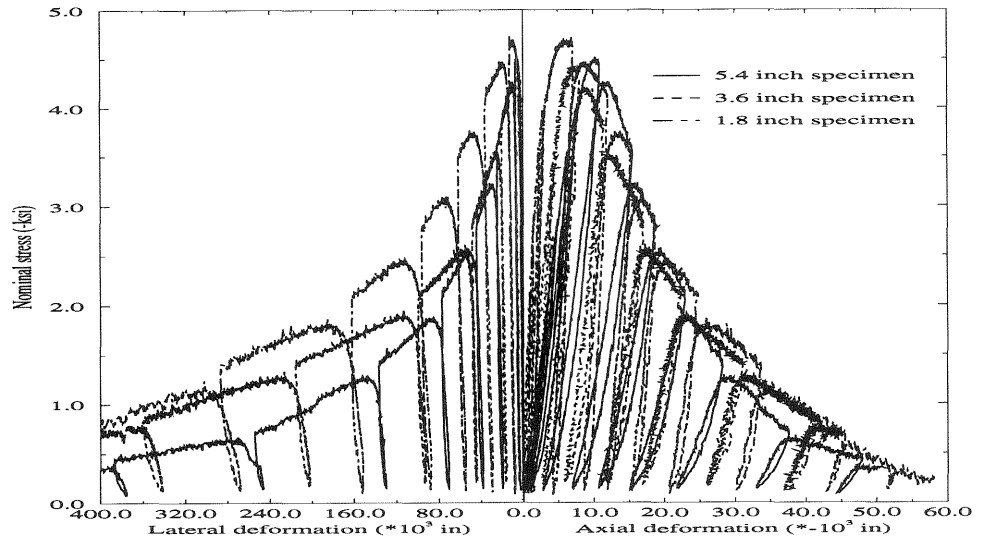


Figure 3: Nominal Stress vs. Axial and Lateral Deformations

eral deformation measurements. Close scrutiny points to a constant ratio between lateral and axial deformations which is much larger than the elastic Poisson's ratio and which may be called a "fictitious Poisson's ratio". It intrigues that the axial deformations are proportional to the lateral deformations irrespective of specimen height. This leads to an important observation that energy dissipation measured along axial direction is transferred directly into lateral crack expansion at constant fracture energy release rate. It is interesting to note that the ratio between the lateral and axial deformations is about $u_l/u_a = 12$ for all specimen heights which is in accordance of factor 8 to 12 between the uniaxial compressive and the tensile strength. Based on this observation internal tensile stresses induce lateral tensile cracking under traction-free lateral boundary condition which may be explained by microstructural arguments of cement paste-aggregate composites. For more insight we consider the response of the 5.4 in height specimen in Fig. 5.

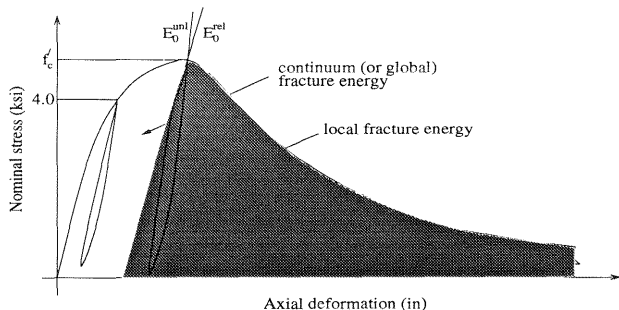


Figure 4: Continuum (Global) and Local Fracture Energies

The ratio between lateral and axial deformation remains constant starting at $u_a = -15 \times 10^{-3}$ in axial compaction, which approximately corresponds to the inflection point in the post-peak regime

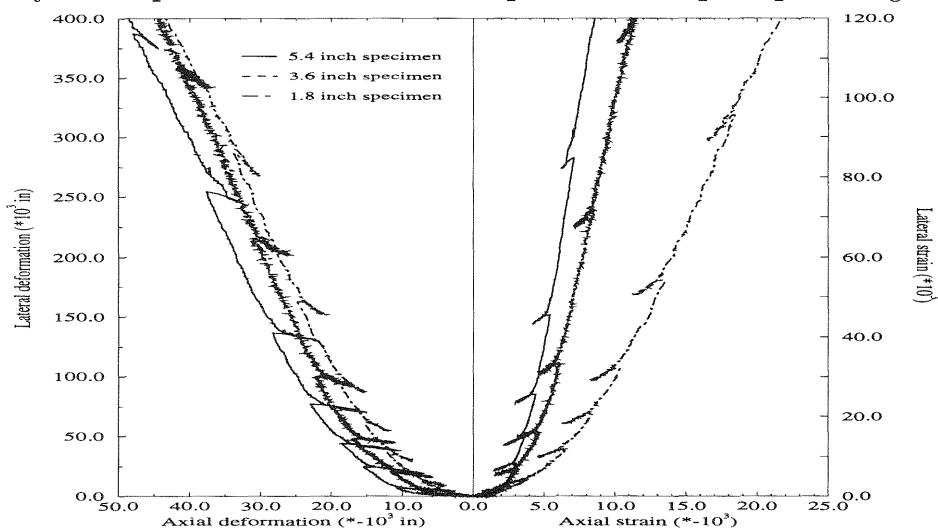


Figure 5: Lateral vs. Axial Deformation and Lateral vs. Axial Strain Response

when $\sigma_a = -3.3$ ksi. If we recall that localized cracking is formed at peak strength, energy dissipation in this range is the combined effect of axial splitting and plastic shear dissipation. This is why the slope between lateral and axial deformations shows the extreme transition of $\nu = 0.18$ in the pre-peak and $\nu_{def} = 12$ in the post-peak regime. When passing through $\sigma_a = -3.3$ ksi, the fracture process results in purely lateral expansion of vertical cracking very similar to the tensile test. If we assume that the plastic energy dissipation due to axial splitting is much larger than that due to shear faulting, a constant characteristic length corresponding to the specimen

height averages the latter part of the softening regime.

3.2 Stiffness degradation

3.2.1 Pre-peak regime

Unloading and reloading stiffnesses were measured at the nominal stress level of $\sigma_a = 2.0, 3.0, 3.5,$ and 4.0 ksi for the three specimen heights. Up to 85% of peak strength all stiffness showed the same properties shown in Table 1. Table 1 indicates that the reloading stiffness at peak level is reduced to 76% which is the average of three different specimens, while unloading stiffnesses show little changes. According to Slate and Hover (1984) the mortar cracks are bridged between bond cracks at 70% to 90% of peak strength. Subsequently cracks coalesce as the stress is further increased, elastic damage in terms of unloading stiffness is negligible, while elastic damage in terms of reloading stiffness is significant due to progressive microcrack formation.

3.2.2 Post-peak regime

The degradation properties in the post-peak regime are described in terms of stiffness-strength, stiffness-fracture energy, and stiffness-plastic deformation.

(a) Stiffness versus Strength: The stiffness degradation during unloading and reloading is shown in Fig. 6(a) for the three specimen heights plotting normalized stiffness (E_d/E_0) versus normalized axial strength (σ_c/f'_c) respectively, where E_0 refers to the stiffnesses at peak. The linear degradation relationship between normalized stiffness and the corresponding strength values is striking.

(b) Stiffness versus Fracture Energy: The normalized fracture energy ($G_f^c/G_{f_{max}}^c$) values are shown in Fig. 6(b) which depicts linearity between G_f^c and the normalized stiffness. Thereby the local fracture energy was evaluated in terms of the areas under the axial stress-deformation curves between unloading (reloading) stiffness at peak strength and that at unloading. Here $G_{f_{max}}^c$ denotes the total fracture energy of the entire softening regime.

(c) Stiffness versus Plastic Deformation: Finally, the stiffness degradation is plotted versus normalized permanent deformation in Fig. 6(c). The permanent deformation at the unloading point was nor-

malized by the total permanent deformation at the last loading cycle, while all permanent deformations were zeroed at peak strength. This data reduction led to a hyperbolic relationship between stiffness and plastic deformation which is single-valued for all three specimen heights.

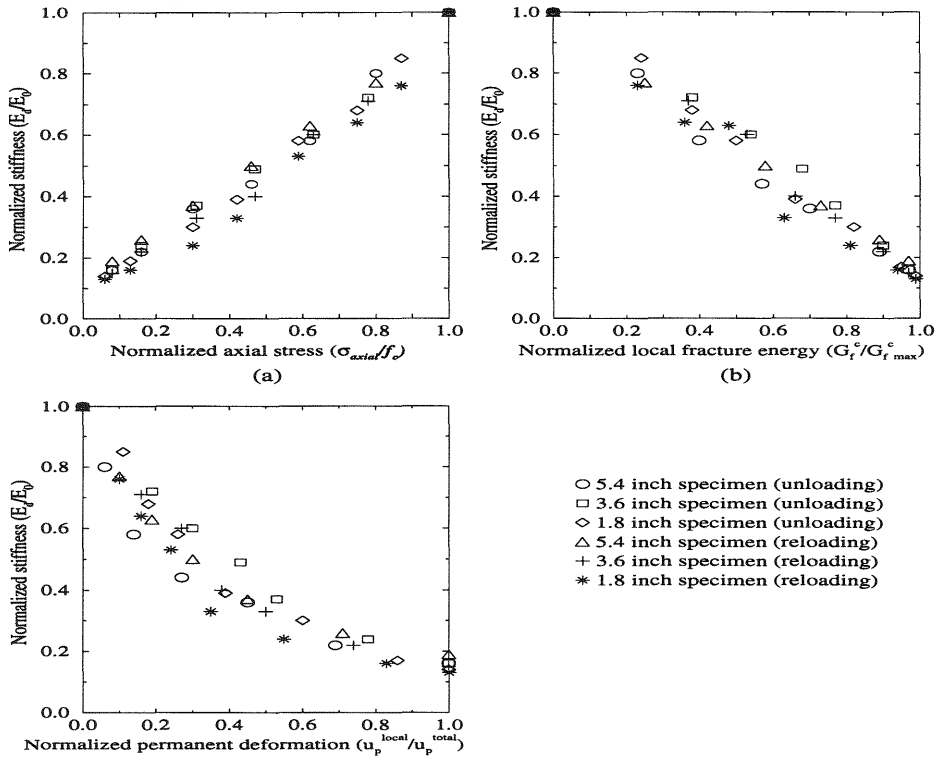


Figure 6: Compressive Concrete Response: (a) Stiffness versus strength, (b) Stiffness versus Fracture Energy, and (c) Stiffness versus Permanent Deformation

3.3 Focal point

The issue, whether there exists a unique focal (pole) point of stiffness degradation is essential for a coherent description of elastic degradation in concrete. A simple analytical procedure is proposed based on experimental observation to determine the location of the focal point, see Fig. 7. In the plot ϵ_{p1} denotes the permanent strain at peak strength, ϵ_{p2} the plastic strain of the peak strength to the current stress σ , ϵ_e the elastic recovery strain, ϵ the total strain, $E(\epsilon)$ the degrading secant modulus of elasticity, E_{max} the modulus of elasticity at peak strength, and σ_{max} the peak strength. If we assume existence of a focal point in the stress-strain plane, the secant

stress-strain relation may be expressed as follows:

$$\sigma - \sigma_0 = E(\epsilon)(\epsilon - \epsilon_0) \quad (1)$$

where $\epsilon = \epsilon_e + \epsilon_{p1} + \epsilon_{p2}$, and $\epsilon_{p1} = \text{constant}$. In order to find the unknown initial strain and stress values, ϵ_0 and σ_0 , in Eqn. (1) one more equation is required. From the initial condition of σ - ϵ diagram marked as line (a) in Fig. 7, the following expression is derived

$$\sigma_0 = \sigma_{max} - E_{max}(\epsilon_e + \epsilon_{p1} - \epsilon_0) \quad (2)$$

where $\epsilon_{p2} = 0$. The values of ϵ_e and ϵ_{p2} are determined from the experimental observations in Fig. 6. The linear relation of stiffness and strength in Fig. 6(a) may be cast into

$$\frac{E}{E_{max}} = a \frac{\sigma}{\sigma_{max}} \quad (3)$$

where a defines the slope between $\frac{E}{E_{max}}$ and $\frac{\sigma}{\sigma_{max}}$. The relation be-

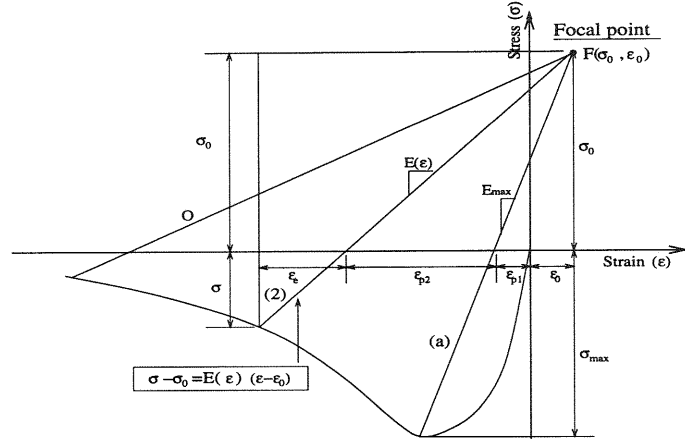


Figure 7: Illustration of a Focal Point

tween stiffness and plastic deformation may be approximated by the hyperbolic relation in Fig. 6(c):

$$\frac{E}{E_{max}} = \frac{c}{\frac{\epsilon_p}{\epsilon_p^{max}} + c}, \quad \epsilon_p = c\epsilon_p^{max} \left(\frac{E_{max}}{E} - 1 \right) \quad (4)$$

where c is a parameter which is calibrated from experiments. From the geometry of triangle (2) in Fig. 7 the secant stress-strain relation yields $\epsilon_e = \frac{\sigma}{E}$. Combining Eqn. (3) and the hyperbolic formulation in Eqn. (4) and the geometry of Fig. (7), ϵ_e and ϵ_{p2} may be

evaluated as follows:

$$\epsilon_e = \frac{1}{a} \frac{\sigma_{max}}{E_{max}}, \quad \epsilon_{p2} = \epsilon_p = c\epsilon_p^{max} \left(\frac{E_{max}}{E} - 1 \right) \quad (5)$$

It is interesting to note that $a = 1$ based on Eqn. (3) and (5) which agrees well with the plot in Fig. 6(a) due to the linear relationship between stiffness and strength degradation.

The determination of the focal point reduces the solution of the two Eqns. (1) and (2) with respect to ϵ_0 and σ_0 . Since $\sigma_{max} = E_{max}\epsilon_e$ and from the geometry in Fig. 7,

$$\epsilon_0 \left(\frac{E_{max}}{E} - 1 \right) = \epsilon_{p1} \left(\frac{E_{max}}{E} - 1 \right) - \epsilon_{p2} \quad (6)$$

It is noted in Eqn. (6) that ϵ_{p2} has to be a function of $\left(\frac{E_{max}}{E} - 1 \right)$ in order to cancel on both sides, otherwise a unique focal point can not be found. Because of that, ϵ_{p2} was characterized by hyperbolic expression in Eqn. (4), which leads to the initial strain

$$\epsilon_0 = \epsilon_p^0 - c\epsilon_p^{max} \quad (7)$$

where $\epsilon_p^0 = \epsilon_{p1}$, is constant. Substituting Eqn. (5) and (8) into (2) leads to the initial stress

$$\sigma_0 = -cE_{max}\epsilon_p^{max} \quad (8)$$

Substituting Eqns. (7) and (8) into (1), the generalized secant formulation for σ is

$$\sigma = E_d(\epsilon) \left[\epsilon - \epsilon_p^0 + cE_{max}\epsilon_p^{max} \right] - cE_{max}\epsilon_p^{max} \quad (9)$$

where $E_d(\epsilon) = E(\epsilon)$. Furthermore, the permanent strain ϵ_p and the degradation modulus of elasticity $E_d(\epsilon)$ can be expressed using Eqns. (3) and (9) as follows:

$$\epsilon_p = c\epsilon_p^{max} \left(\frac{E_{max}}{E} - 1 \right) + \epsilon_p^0, \quad E_d(\epsilon) = \frac{cE_{max}\epsilon_p^{max}}{\epsilon - \epsilon_p^0 + c\epsilon_p^{max} - \frac{\sigma_{max}}{E_{max}}} \quad (10)$$

For verification the proposed procedure to determine a unique focal point Eqns. (7), (8), (9), and (10) are used to predict the behavior of the $h = 5.4$ in specimen. From regression analysis of three specimen heights the mean value of c is known to be 0.261 and 0.287 for reloading and unloading stiffnesses, respectively, and $c = 0.286$ for reloading in the case of the $h = 5.4$ in specimen. The permanent strain $\epsilon_p^0 = -0.66 \times 10^{-3}$, the maximum permanent strain

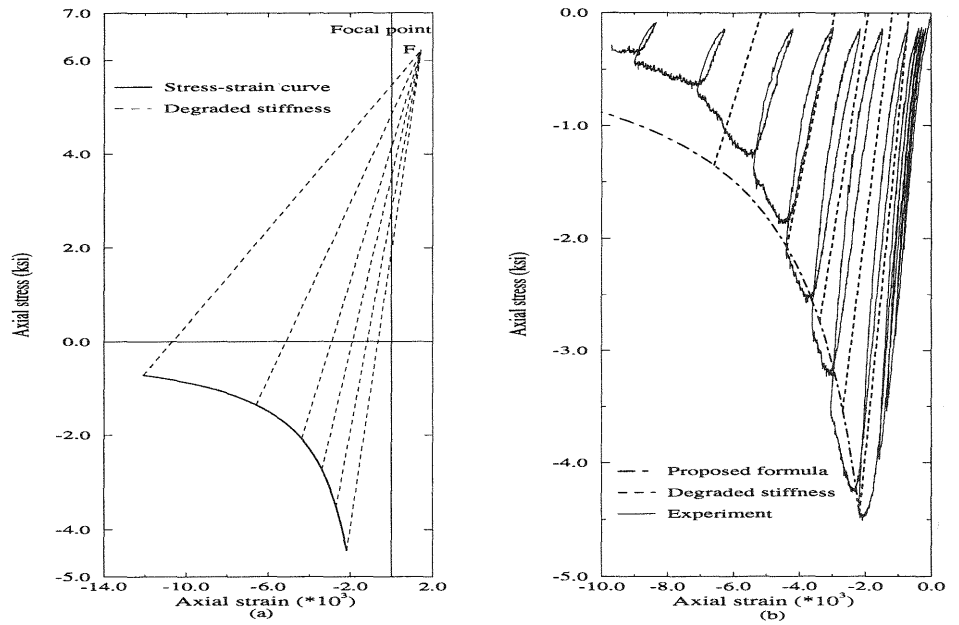


Figure 8: Comparison of Focal Point with Experimental Result: (a) Focal Point of 5.4 Inch Specimen and (b) Comparison of Focal Point with 5.4 inch Specimen

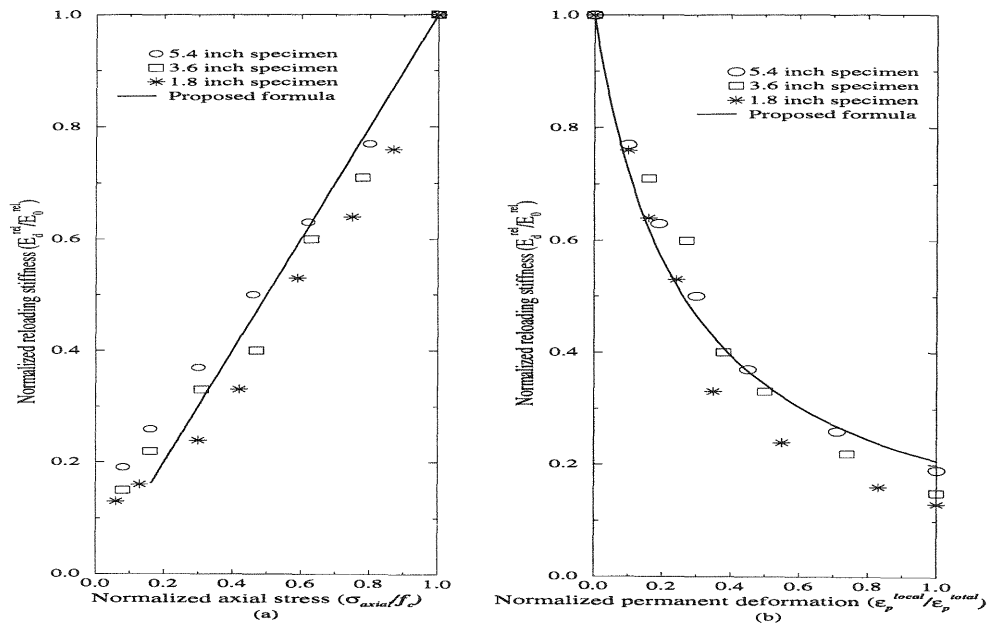


Figure 9: Experimental Result Predicted with the Proposed Formula for Focal Point: (a) Prediction of Fig. 6(a) and (b) Prediction of Fig. 6(c)

$\epsilon_p^{max} = -7.39 \times 10^{-3}$, the modulus of elasticity measured at the peak strength $E_{max} = 2940$ ksi, and the peak strength $\sigma_{max} = -4.45$ ksi. With the above input data from experimental results of the tall specimen, $\epsilon_0 = 1.45 \times 10^{-3}$ and $\sigma_0 = 6.21$ ksi using Eqns. (7) and (8). Fig. 8 shows the predicted stress-strain diagram and the degrading modulus of elasticity for comparison with the experimental result of the $h = 5.4$ in specimen. The discrepancy of stress-strain curve in Fig. 8(b) is due to the linear approximation (slope=1) of the relation between the degradation modulus and the degradation strength. Note that zero values of the residual strength, when $\sigma = 0$, does not infer that $E_d=0$ according to the experimental result (see Fig. 6(a)). However, E_d of the proposed formula agrees well with the experimental result of the same strength level because the calibrated c value is almost identical with the experimental result. In sum Fig. 9 illustrates the experimental results of Fig. 6 for comparison with the proposed generalized secant expression with the focal point $F(\sigma_0, \epsilon_0)$. The proposed procedure readily extends to 3-D formulation to incorporate the effect of confinement when c , σ_0 and ϵ_0 are expressed as functions of confining pressure.

4 Brittle failure in compression

Decohesive tensile cracking is a common failure mode of many brittle materials. Even under all-around compressive loadings, microdefects such as cavities, pores, grain boundaries, inclusions, and other inhomogeneities, enable brittle materials to fail due to tensile microcracking. Under large confining pressure, brittle materials such as rocks, ceramics, and concrete may undergo plastic flow accompanying microcracking, so that the plastic deformation should be the dominant dissipation mechanism. However, they might not even reach the plastification before rupture under small amount of confining pressure. The experiments above did demonstrate that axial splitting under uniaxial compression is caused by nucleation at tensile flaws which grow in the direction of compression. In order to verify the axial splitting failure under uniaxial compression, the sliding crack model, initially proposed by Brace and Bombolakis (1963), and later quantified analytically and confirmed experimentally by Nemat-Nasser and Hori (1982), is adopted. The model assumes a

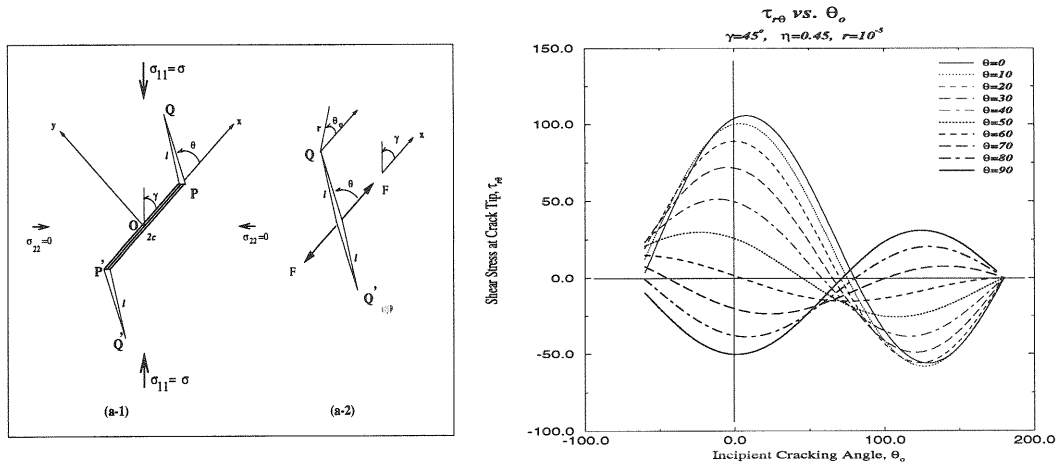


Figure 10: (a-1) Preexisting flaw PP' and straight cracks PQ & $P'Q'$, (a-2) A representative tension crack QQ' with splitting forces F , (b) $\tau_{r\theta}$ vs. θ_o when $\gamma = 45^\circ$

preexisting flaw with suitable inclination $\gamma \neq 0$ and curved tensile cracks under biaxial compression. However since the numerical calculations are very laborious for curved cracks, they were substituted with equivalent straight cracks; Hori and Nemat-Nasser (1986) as shown in Fig. 10(a).

A 2-d elasticity boundary-value problem associated with the model shown in Fig. 10(a-1), was formulated in terms of singular integral equations and solved numerically, see Nemat-Nasser and Hori (1982). The boundary conditions on the flaw PP' are $u_y^+ = u_y^-$, $\tau_{xy}^+ = \tau_{xy}^- = -\tau_c + \eta\sigma_y$, where τ_c denotes the cohesive stress, η the frictional coefficient in a range of 0.3-0.6, u_y the displacement in the y -direction, σ_y the normal stress, and τ_{xy} the shear stress on PP' . Under uniaxial compression, if small amount of lateral tension is applied, then the crack grows in an unstable manner after a certain crack extension is attained. The unstable crack growth is a fundamental micromechanism of axial splitting of a uniaxially compressed brittle specimen.

In Fig. 10(a-2), the force F represents the effect of the preexisting flaw on cracks PQ and $P'Q'$. The crack QQ' is a hypothetical crack representing cracks at the flaw tips, which are subjected to force F caused by a frictional motion of the preexisting flaw, and subjected to farfield compressive stresses σ . The force F is estimated from the

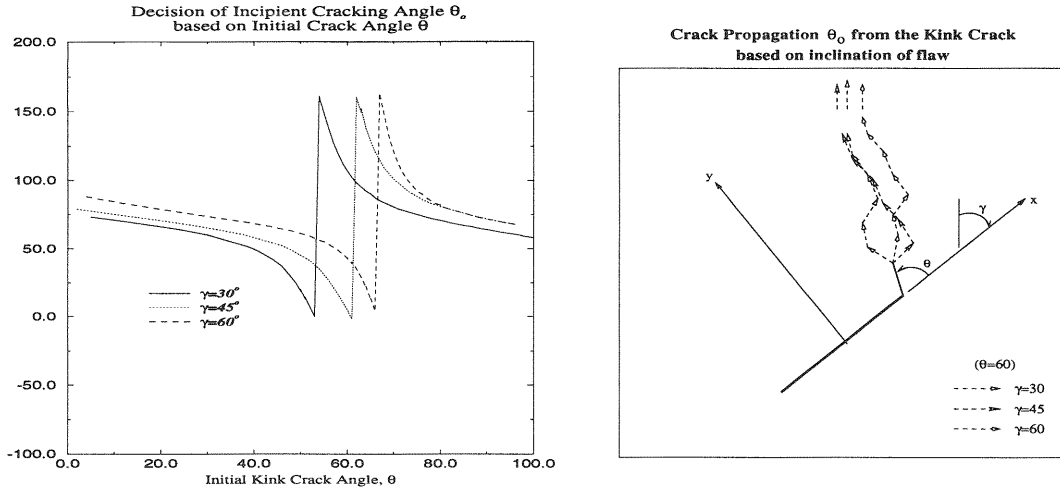


Figure 11: (a) Graph to obtain the incipient cracking angle, θ_0 , (b) Crack Propagation

driving shear stress τ^* , on the preexisting flaw P'P'

$$\tau^* = -\frac{1}{2}\sigma \sin 2\gamma - \tau_c + \frac{1}{2}\eta\sigma\{1 - \cos 2\gamma\} \quad (11)$$

Under the concentrated coaxial forces $F = 2c\tau^*$ and the farfield stress σ , the stress intensity factors at Q and Q' are

$$K_I = \frac{2c\tau^* \sin \theta}{\sqrt{\pi(l+l^*)}} + \frac{1}{2}\sqrt{\pi}l\sigma\{1 - \cos 2(\theta - \gamma)\}, \quad K_{II} = \frac{-2c\tau^* \cos \theta}{\sqrt{\pi(l+l^*)}} - \frac{1}{2}\sqrt{\pi}l\sigma \sin 2(\theta - \gamma) \quad (12)$$

In this equation, l^*/c is assumed to be 0.27 (where, l^* is an imaginary length to take care of preexisting flaw into the crack QQ') to allow accuracy of the equation even when l is vanishingly small. The crack tip stresses, σ_r , σ_θ , and $\tau_{r\theta}$ in polar coordinate system, are introduced in order to determine the incipient crack angle, θ_0 . Assuming that cracking progresses in the direction normal to the maximum normal stresses (i.e. Max. Eigenvalues), the incipient angle, θ_0 can be determined by setting shear stresses, $\tau_{r\theta}$ to zero. After some manipulation, $\tau_{r\theta}$ becomes

$$\begin{aligned} \tau_{r\theta} = & \frac{1}{\sqrt{2\pi r}} \left[\left\{ \frac{2c\tau^* \sin \theta}{\sqrt{\pi(l+l^*)}} + \frac{1}{2}\sqrt{\pi}l\sigma(1 - \cos 2(\theta - \gamma)) \right\} \sin \frac{\theta_0}{2} \cos^2 \frac{\theta_0}{2} \right. \\ & \left. + \left\{ \frac{-2c\tau^* \cos \theta}{\sqrt{\pi(l+l^*)}} - \frac{1}{2}\sqrt{\pi}l\sigma \sin 2(\theta - \gamma) \right\} \left(\frac{1}{4} \cos \frac{\theta_0}{2} + \frac{3}{4} \cos \frac{3\theta_0}{2} \right) \right] = 0 \quad (13) \end{aligned}$$

The incipient angle, θ_0 is, therefore, obtained by plotting $\tau_{r\theta}$ vs. θ_0 with the kink crack angle θ changing from 0° to 90° as shown in Fig. 10(b) for $\gamma = 45^\circ$. As seen in Fig. 11(a), the incipient angle, θ_0 changes with the initial kink crack angle, θ , it curves toward the direction of principal compressive stress, and grows with increasing

compression, eventually aligning parallel to the direction of compressive loading, see Fig. 11(b). The plot in Fig. 11(a) is obtained based on graphs like the one shown in Fig. 10(b) for different γ values. Assuming that the inclination angle $\gamma = 45^\circ$ and the kink crack angle $\theta = 60^\circ$, the incipient angle $\theta_o^{(1)}$ is determined as 5° from Fig. 10(b) or 11(a). By the same token, the next incipient angle $\theta_o^{(2)}$ is attained as 77° , and the third one as 85° . After a number of processes, the crack propagates to the direction of compressive loading. In this manner, the axial splitting failure mode of brittle solids is attained in uniaxial compression in a fracture-micromechanical interpretation.

5 Concluding remarks

Uniaxial compression tests were performed under displacement control on cylindrical concrete specimens of different height. Degradation of stiffness and strength were measured during unloading and reloading cycles. The unloading and reloading stiffnesses were correlated to strength degradation, local fracture energy, and permanent deformations. Specimens of different height were used in order to investigate fracture effects of concrete in compression. Special provisions were made to minimize interface friction. The degradation measurements of stiffness, strength and local fracture energy were single-valued throughout the experiments of different height specimens. Compressive concrete softening was shown to support fracture energy concepts irrespective of specimen height and the issue of characteristic length was addressed through experimental observations. Finally a procedure to determine a unique focal point was proposed and compared with experimental data, and the axial splitting mode of compression failure was explained with the aid of fracture mechanics concepts.

Acknowledgements

The first two authors wish to thank Dr. Slowik for his advice during experiments. They are grateful for the financial support of the US-AFOSR under grant 49620-92-J-0442 to the University of Colorado Boulder.

References

- Brace, W.F. and Bombolakis, E.G. (1963) A note on brittle crack growth in compression. **J. Geophys. Res.**, 68, 3709-3731.
- Hori, H. and Nemat-Nasser, S. (1986) Brittle failure in compression: splitting, faulting, and brittle-ductile transition. **Phil. Trans. Roy. Soc. Lond.**, 319, 1549, 337-374.
- Nemat-Nasser, S. and Hori, M. (1993) **Micromechanics: Overall Properties of Heterogeneous Materials**. North-Holland.
- Rokugo, K. and Koyanagi, W. (1992) Role of compressive fracture energy of concrete on the failure behavior of reinforced concrete beams, in **Applications of Fracture Mechanics to Reinforced Concrete** (ed. A. Carpinteri), Elsevier Applied Science, London, 437-464.
- Sinha, A., Gerstle, K.H., and Tulin, L.G. (1964) Stress-strain relations for concrete under cyclic loading. **J. Am. Concr. Inst.**, 61, 2, 195-211.
- Slate, F.O. and Hover, K.C. (1984) Microcracking in concrete, in **Fracture Mechanics of Concrete** (eds A. Carpinteri and A. R. Ingraffea), Martinus Nijhoff Publishers, The Hague, 137-159.
- Slowik, V., Alvaredo, A.M., and Wittmann, F.H. (1993) Experimental and numerical investigation into the probabilistic character of crack growth, in **Numerical Models in Fracture Mechanics of Concrete** (ed F.H. Wittmann), A.A.Balkema, Rotterdam, 223-231.
- Van Mier, J.G.M. (1986) Multiaxial strain-softening of concrete, part I: fracture, part II: load-histories. **Materials and Structures, RILEM**, 19 (111), 179-200.
- Vonk, R.A. (1992) Softening of concrete loaded in compression. Ph.D. thesis, Eindhoven University of Technology, The Netherlands.
- Willam, K., Hurlbut, B., and Sture, S. (1986) Experimental and constitutive aspects of concrete failure, **Proc. Finite Element Analysis of Reinforced Concrete Structures**, ASCE Special Volume, New York, 226-254.